ADVANCED INTELLIGENT SYSTEMS
Open Access
www.advintellsyst.com

SensAct: The Soft and Squishy Tactile Sensor with Integrated Flexible Actuator

*Oliver Ozioko, Prakash Karipoth, Pablo Escobedo, Markellos Ntagios, Abhilash Pullanchiyodan, and Ravinder Dahiya**

Herein, a novel tactile sensing device (SensAct) with a soft touch/pressure sensor seamlessly integrated on a flexible actuator is presented. The squishy touch sensor is developed with custom-made graphite paste on a tiny permanent magnet, encapsulated in Sil-Poxy, and the actuator (15 μ-thick coil) is fabricated on polyimide by Lithographie Galvanoformung Abformung (LIGA) micromolding method. The actuator can operate in two modes (expansion and contraction/squeeze) and two states (vibration and nonvibration). The sensor was tested with up to 12 N applied forces and exhibited ≈70% average relative resistance variation ($\Delta R/R_o$), ≈0.346 kPa^{-1} sensitivity, and ≈49 ms response time with excellent repeatability (≈12.7% coefficient of variation) at 5 N. During simultaneous sensing and actuation, the modulation of coil current, due to $\Delta R/R_o$ (≈14% at 2 N force) in the sensor, allows the close loop control ($\Delta I/I_o$ ≈385%) of expansion/contraction (≈69.8 μm expansion in nonvibration state and ≈111.5 μm peak-to-peak in the vibration state). Finally, the soft sensor is embedded in the 3D-printed fingertip of a robotic hand to demonstrate its use for pressure mapping along with remote vibrotactile stimulation using SensAct device. The self-controllable actuation of SensAct could provide eSkin the ability to tune stiffness and the vibration states could be utilized for controlled haptic feedback.

1. Introduction

Flexible pressure sensors are increasingly being explored for electronic skin (eSkin)[1] and their application in soft robotics,[2] medical, sensory substitution for prosthesis,[3] rehabilitation, etc.[4] As a result, different types of flexible touch and pressure sensors have been reported using various materials,[5] structures,[6] morphology,[7] and transduction methods.[8] Some of these have also mimicked human skin features such as fingertip-like patterns on skin surface and integrated static and dynamic sensors. However, complexity of eSkin goes beyond just integrating few types of touch sensors on flexible substrates.[9] Intrinsic or tightly integrated touch sensing, actuation, and computation into soft 3D structures[10] is a salient feature of human skin[11] which also helps to tune some of the functionalities (e.g., softness).[1e] eSkin with such features could enable a new generation of truly smart and complex systems such as robots having human like dexterity, cognitive skills, and physical abilities that rely on feedback provided by various receptors in the body. In this context, various types of actuators (e.g., electromagnetic,[12] pneumatic,[13] and electroactive polymers [EAPs],[14] etc.) have also been explored.[15] However, except the electromagnetic and ionic EAPs,[16] the majority of actuators are unable to provide bidirectional actuation needed to create vibrotactile feedback.[17] Due to bulky size and large voltages needed to create movements, even these actuators are difficult to be used in a soft and squishy eSkin along with distributed touch sensors. By integrating tactile sensors and actuator in a single structure, herein, we present a novel soft and squishy device (SensAct) as the building block for advanced eSkin which will provide localized vibrotactile feedback. Such integrated SensAct devices are needed in applications such as prosthesis and deaf-blind people communication, where tactile sensors and actuators are currently utilized separately.[18]

The SensAct device (**Figure 1**a) presented here comprises a soft piezoresistive pressure sensor integrated on top of a flexible electromagnetic coil-based actuator. This arrangement allows the device to simultaneously detect the contact pressure as well as actuate the top surface of the devices up or down (i.e., expand or contract/squeeze the soft device). The fabricated device has been characterized individually for piezoresistive tactile sensing (second layer from top in Figure 1a) as well as complete SensAct device (Figure 1a). In the effort to make the structure intrinsically soft and squishy, we have used flexible magnets and elastomers mixed with ferromagnetic materials for the purpose of actuation.[19] The electromagnetic actuators have so far been mainly been used for actuation purposes,[20] with

Dr. O. Ozioko, Dr. P. Karipoth, Dr. P. Escobedo, M. Ntagios, Dr. A. Pullanchiyodan, Prof. R. Dahiya
Bendable Electronics and Sensing Technologies (BEST) Group
James Watt School of Engineering
University of Glasgow
G12 8 QQ Glasgow, UK
E-mail: Ravinder.Dahiya@glasgow.ac.uk

The ORCID identification number(s) for the author(s) of this article can be found under https://doi.org/10.1002/aisy.201900145.

DOI: 10.1002/aisy.201900145

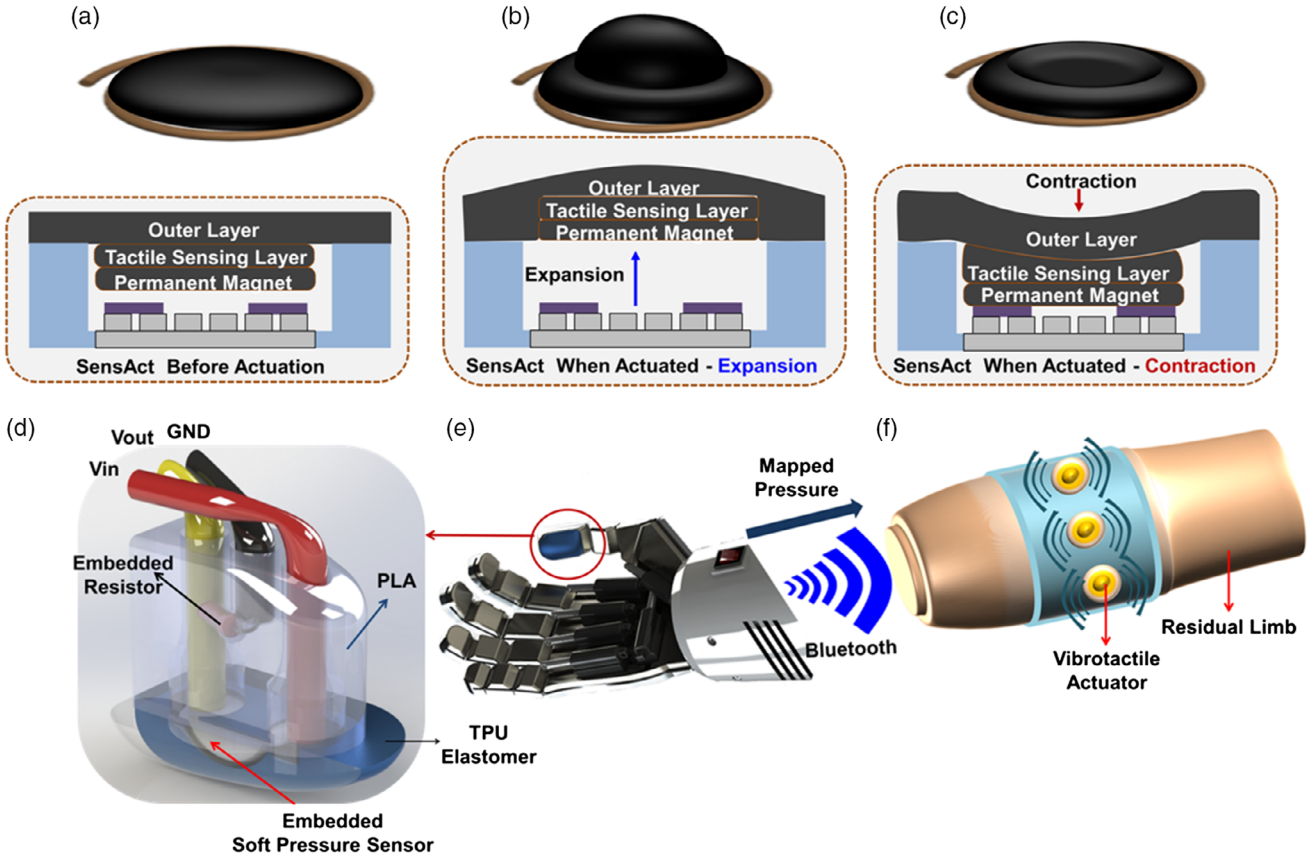

Figure 1. a) Structure of SensAct device—No actuation; b) SensAct during actuation—expansion; c) SensAct during actuation—contraction; d) Structure of the 3D-printed fingertip with embedded soft sensor; e) Prosthetic hand with integrated soft piezoresistive sensor; f) Residual limb with vibrotactile actuator.

primary applications in micropumps,[21] and tactile displays.[22] In this regard, the actuator with intrinsic touch sensing presented here through SensAct device is a significant advance.

Figure 1a shows SensAct before actuation; during actuation, the top layer expands, or contracts, as shown in Figure 1b,c respectively. In this article, these different actuation modes and states of SensAct are demonstrated. As a proof of concept, a piezoresistive sensor was embedded into a custom 3D-printed prosthetic distal phalanx (Figure 1d) of the thumb to demonstrate the potential application of SensAct in pressure sensing with vibrotactile feedback in a prosthetic hand (Figure 1e,f).

2. Working of SensAct

Figure 2 shows the structure and working principle of the sensing and actuating parts of SensAct. Sensing is achieved by means of piezoresistive effect while actuation is achieved through electromagnetic force which occurs as a result of the interaction between the magnetic field of the coil and the permanent magnet. Figure 2a1,a2 shows the structure of the piezoresistive sensing layer before and after external contact, respectively. The piezoresistive sensing element was fabricated using a custom-made graphite paste applied as a thin layer on a permanent magnet encapsulated in an elastomer. Before pressure is applied (Figure 2a1), the graphite particles in the paste are randomly distributed within the elastomer in such a way that any two arbitrary particles occupy certain fixed position in space (say d_1 and d_2 in (Figure 2a1). Upon application of external pressure, the embedded particles come closer (by Δd_1 and Δd_2) to form conducting paths and thereby decreasing the effective electrical resistance, R (Figure 2a2). Once the external pressure is released, the elastic restoration of the elastomer occurs; causing the embedded particles to move to their original positions and thus the effective electrical resistance is restored to its original value. The amount of applied pressure can be estimated by measuring the change in resistance, ΔR.

Figure 2b,c shows the structure and working of SensAct with two distinct layers—1) the piezoresistive sensing layer and 2) the actuating layer; both of which systematically interact to provide controllable sensing and actuation (Figure 2c). The actuating element consists of a flexible spiral coil and a thin permanent magnet. Actuation occurs when current (constant or pulsating) is supplied through the coil, causing an interaction of the magnetic field produced by the coil and the magnet, as shown in Figure 2b.

Depending on the direction of current flow, this magnetic interaction creates two actuation modes (contraction and expansion modes) with reference to the movement of the top layer to the coil. SensAct operates in contraction mode when the magnet

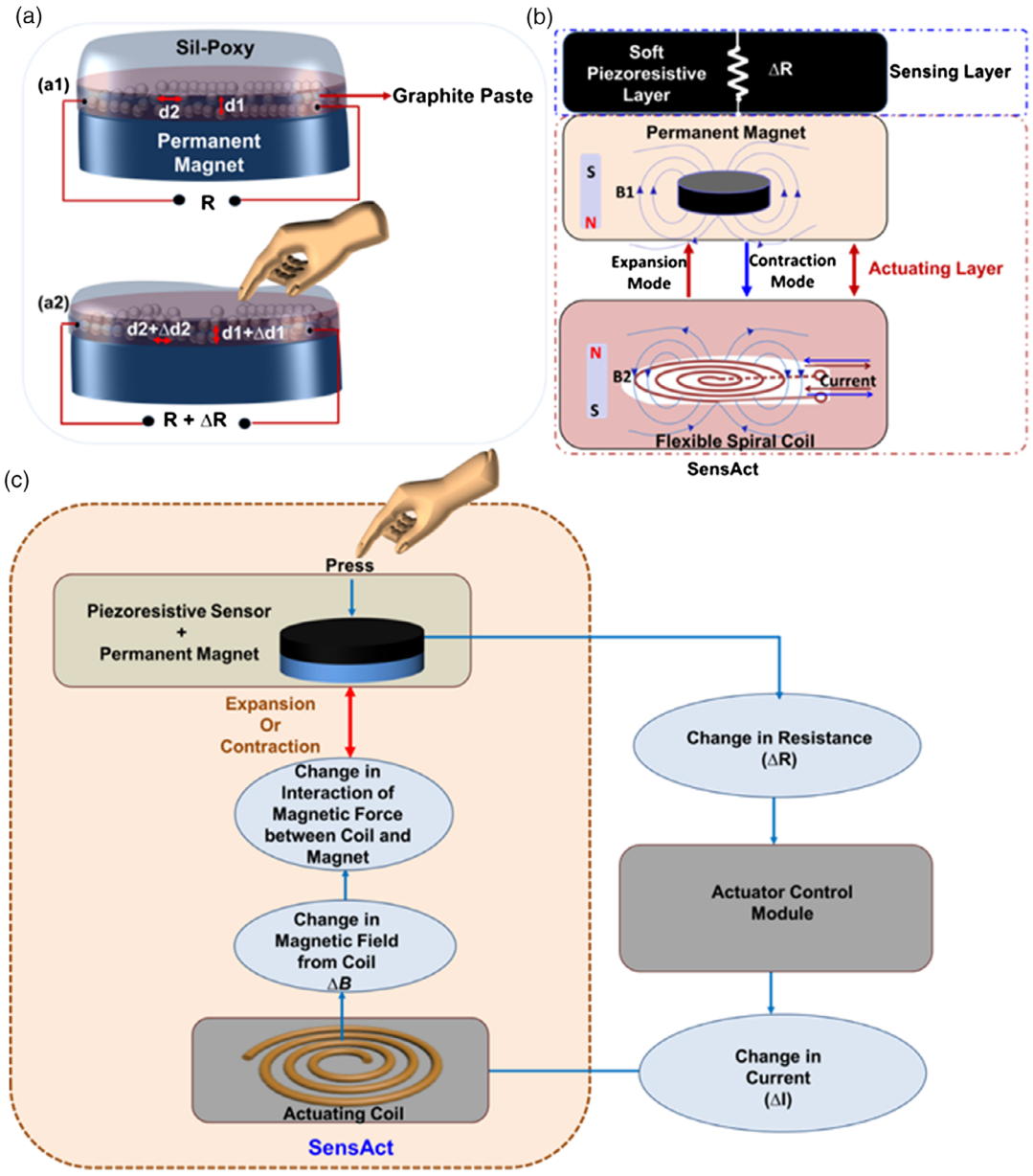

Figure 2. a) SensAct showing the structure and principle of the piezoresistive layer; b) SensAct showing the structure and principle of the actuation layer; c) block diagram showing the principle of SensAct's simultaneous sensing and actuation.

(and sensing layer) is attracted toward the coil. If the magnet (and sensing layer) is repelled away from the coil, SensAct operates in expansion mode (Figure 2b). In each mode there are two possible states—vibration state and nonvibration state—depending on the nature of the supplied current. When a constant current is supplied during each of these modes, the magnet (and sensing layer) stay in the actuated position until current is off. To create vibration, a pulsating current at a certain frequency is supplied to the actuator instead of constant current, causing the top layer to move up (expand) and down (contract) periodically in accordance with the frequency of the pulse. This is advantageous given that the speed, movement and direction of the top layer can be manipulated by the magnitude and direction of the supplied current. The sensing and actuation operations of SensAct device could be independent or simultaneous in a closed loop mode. In this work, we have implemented simultaneous control of sensing and actuation as shown in Figure 2c. In this implementation, the resistance of the sensing layer is used as a variable current-limiting element in the actuator control module. This modulates the amount of current utilized in driving the actuating coil during operation.

During simultaneous operation of sensor and actuator in SensAct (Figure 2c), an external pressure on the sensing layer results in change in resistance (ΔR). This resistance shift causes a change in the current (ΔI) produced by the actuating control module which is then utilized to drive the actuating coil.

The change of the driving current (ΔI) causes a change in the current flowing through the coil and hence, the magnetic field the coil generates. This change in the magnetic field, changes the interaction of magnetic force (attractive or repulsive) between the coil's magnetic field and the permanent magnet. Consequently, actuation occurs and the sensing layer moves away from the coil (expansion mode) or closer to the coil (contraction mode) depending on the direction of current. This means that the current through the coil can be modulated by the amount of external force on the sensing layer, which in turn controls the position of the sensing layer. Therefore, SensAct leverages the sensing ability of the elastomer and the magnetic interaction between the coil and the embedded tiny permanent magnet to produce simultaneous sensing and actuation. The eSkin with such features could be programmed to respond to an external force (either by moving close to, or away from it), or tuned for other new functionalities such as varying the stiffness of soft layer. Further details of the control mechanism including the actuation control module are shown in Figure S3, Supporting Information.

3. Experimental Section

The experimental section is divided into two main parts 1) fabrication of SensAct and 2) characterization of SensAct, including details of all the modules.

3.1. Fabrication of SensAct

The fabrication of the SensAct device involved three major parts: 1) fabrication of the piezoresistive sensing element; 2) fabrication of the actuating element; and 3) integration of the actuation and sensing elements.

3.1.1. Fabrication of Piezoresistive Sensing Elements

Figure 3 shows the steps for fabricating the piezoresistive pressure sensor. It was fabricated on a commercial 12 mm diameter $\times$ 1 mm thin NdBFe disc magnet (Grade N42, 0.73 kg pull) (Figure 3a) using graphite paste, and Sil-Poxy as the encapsulant. First, a thin insulating adhesive tape was attached to one of the faces of the circular magnet (Figure 3b) to avoid electrical short circuit between the sensor and the conductive metal coating of the magnet. Electrical contacts were made on the insulation layer (Figure 3c) at two diametrically opposite ends using fine copper wires attached with commercial silver paste (RS PRO Silver Conductive Paint) and encapsulated by epoxy (RS PRO Quick Set Epoxy Adhesive Resin). Following this, a thin layer of graphite paste, which was prepared based on the similar approach reported in the study by Ntagios et al.[3c] using Triton X-100 (Sigma Aldrich) as dispersant, terpineol (Sigma Aldrich) as the solvent and ethyl cellulose as the binder, was applied to cover the insulating layer completely (Figure 3d) and was allowed to dry in an oven at 65 °C for 1 h. Afterward, the sensing layer is completely encapsulated along with the permanent magnet using Sil-Poxy silicone adhesive (Figure 3e). After this process, the whole package constituting the magnet and the sensing layer serves as single functional device enabling both sensing and actuation capabilities. A total of four devices were fabricated to validate their repeatability as well as device-to-device performance uniformity (Video S1, Supporting Information).

3.1.2. Fabrication of the Actuating Element

Figure 4 shows the fabrication process of the spiral coil which drives the actuation. The 15 μm-thick spiral coil was fabricated following the Lithographie Galvanoformung Abformung (LIGA) process, as described in our previous work.[23] First,

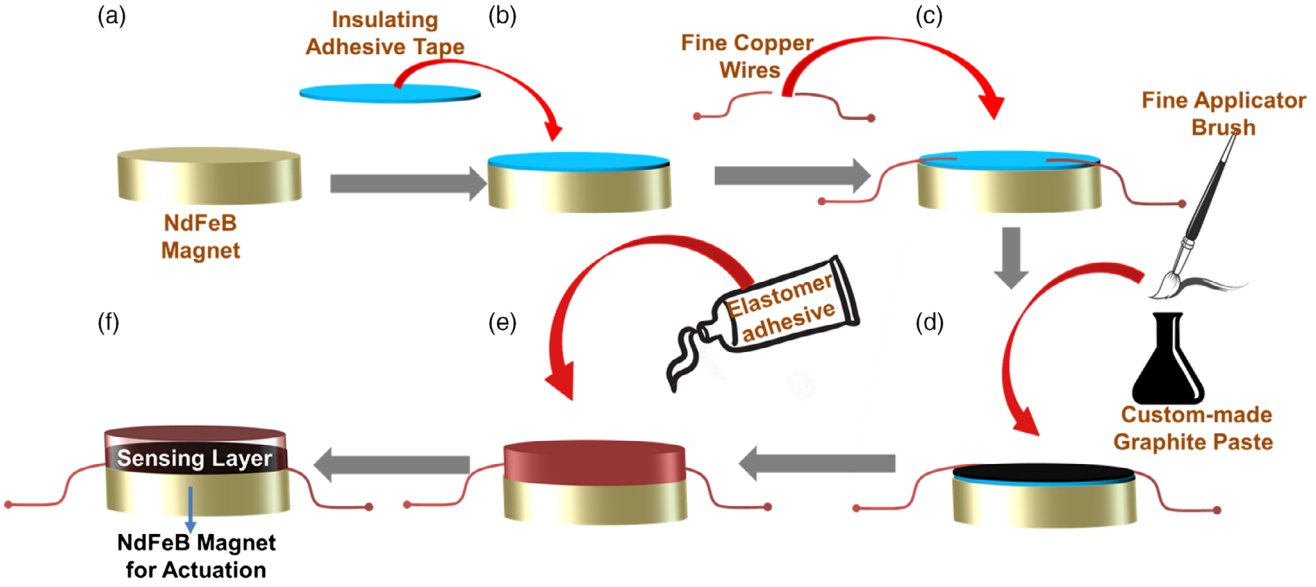

Figure 3. Fabrication steps for the piezoresistive sensing layer a) The thin permanent magnet before fabrication; b) attachment of insulating adhesive tape on the permanent magnet; c) attachment of the fine conducting copper electrodes; d) application of the custom-made graphite paste; e) encapsulation of the sensing layer using Sil-Poxy silicone adhesive; f) wholly encapsulated permanent magnet with integrated sensing layer.

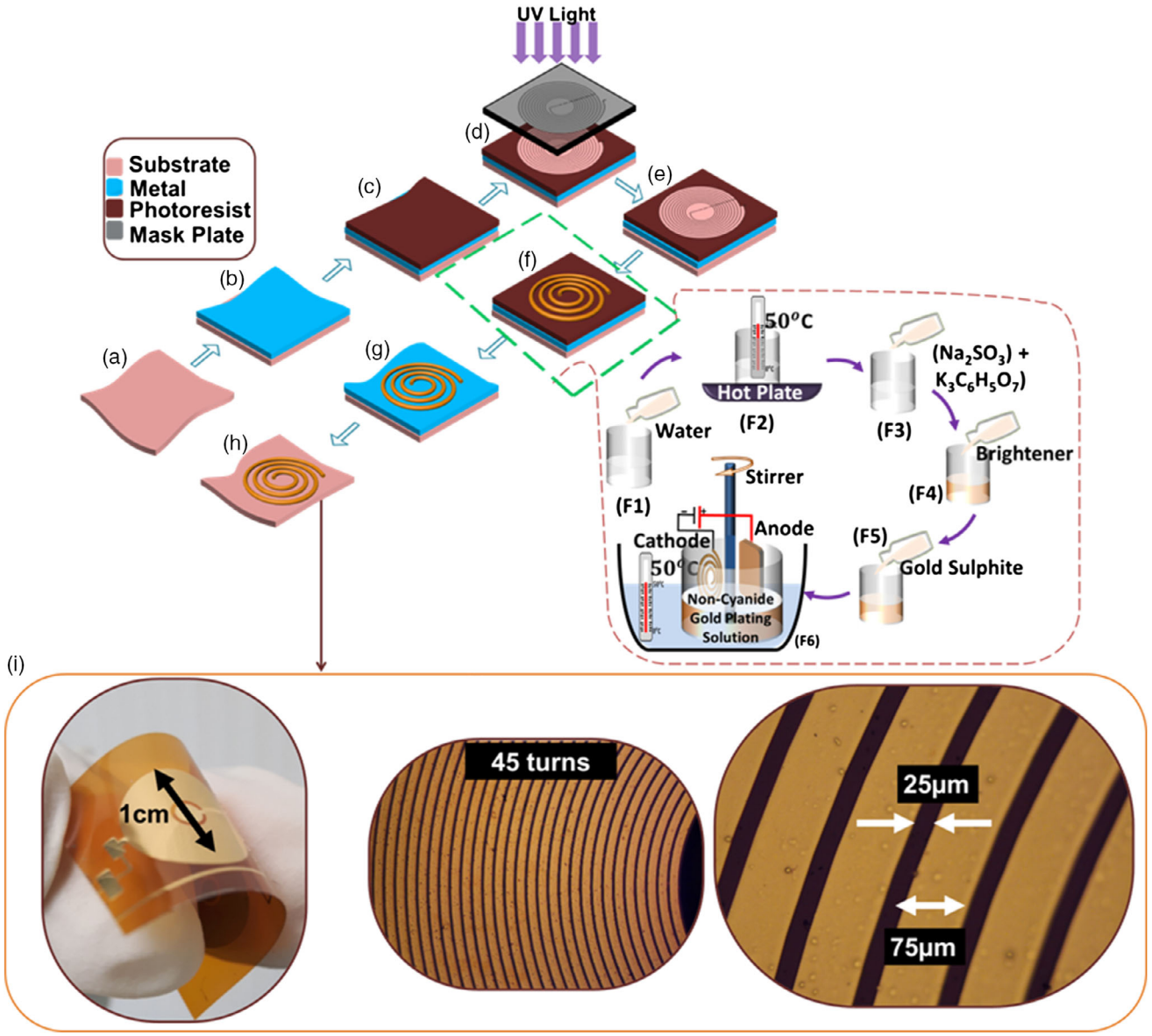

Figure 4. Fabrication steps for the flexible spiral coil: a) flexible polyimide substrate; b) gold deposition using metal evaporation technique; c) spin coating of AZ4562 photoresist; d) exposure of photoresist to UV light during lithography; e) developing the exposed AZ4562 photoresist using AZ826; f) noncyanide gold-plating of the spiral coil; g) lift-off the unwanted photoresist; h) etching of the seed layer; i) fabricated flexible spiral coil for actuation.

10/60 nm NiCr/Au was deposited on a flexible 50 µm polyimide sheet using Plassys MEB 550S Electron Beam Evaporator system. After this, the AZ4562 photoresist was spun at 2000 rpm for 3 s. The sample was then left at room temperature for about 30 min to remove any trapped bubble. Baking of the sample at 100 °C for ≈10 min was carried out, and the resulting sample was left for 30 min to allow further evaporation of the solvents.

The sample was then patterned by exposing it to an ultraviolet (UV) light through a dark-field mask for 60 min, following the standard lithography technique. The exposed sample was then developed using AZ826 developer for 10 min and rinsing in reverse osmosis (RO) water. To increase the thickness of the resulting spiral coil, we electroplated it (Figure 4f) using 1 L of noncyanide gold electroplating solution prepared by mixing Na_2SO_3, tripotassium citrate ($K_3C_6H_5O_7$), 5 mL of brightener (containing arsenic salt), and 50 mL of gold sulfite in RO water (Figure 4f1–f6).

The sample (flexible spiral coil with 45 turns) was then gold-plated using a current density of ≈5 mA cm^{-2} for ≈40 min to achieve ≈15 µm-thick coil by immersing it in the formulated noncyanide gold complex electroplating solution and connecting it to the cathode of a constant current source. Noncyanide gold plating solution was chosen because of its nontoxicity, high plating efficiency, compatibility with photoresists, and controllable residual stress of the plated gold.[24] The unwanted gold layer was then etched using a gold etchant for ≈13 s exposing the

NiCr seed layer. Following this, the sample was annealed at 300 °C in a furnace for ≈20 min under nitrogen ambient. This was a critical step, as the failure may cause undesirable lift-off of the coil pattern. Etching of the NiCr seed layer was then carried out using Nichrome etchant exposing only the required gold-plated spiral pattern (Figure 4h).

3.1.3. Integration of the Sensing and Actuating Elements

Figure 5 shows the steps followed to assemble the fabricated sensing and actuating elements. First, a 50 µm-thick polyimide sheet of $2 \times 2\ cm^2$ (Figure 5a) was prepared and then attached to the spiral coil (Figure 5b) using Loctite adhesive.

This was followed by the attachment of the coil separator to the coil (Figure 5c) to protect it from the magnet, creating ≈100 µm gap between coil and the magnet. One end of two $3.5 \times 2.5\ mm^2$ flexible 80 µm polyvinyl chloride (PVC) film were then attached to the tiny magnet (Figure 5d), which was encapsulated by the piezoresistive layer, as described in Section 3.1.

The other ends of the attached PVC film were used to anchor the magnet to the coil separator. Finally, the entire integrated structure was carefully encapsulated with the initial polyimide sheet using thin layer of Ecoflex from Smooth On and Loctite adhesive (Figure 5e). Figure 5f shows the image of the integrated SensAct with the sensing layer and actuating coil both measuring 1 cm in diameter.

3.2. Characterization of SensAct

The characterization of SensAct involved three main parts: 1) characterization of the piezoresistive sensing module, 2) characterization of the actuating module, and 3) characterization of the integrated sensing and actuation module.

3.2.1. Characterization of the Piezoresistive Sensing Module

The characterization of the piezoresistive sensing elements fabricated in this work (described in Section 3.1.1) was carried out by attaching each device firmly to a stable 1004 aluminum single point low-capacity load cell, which can measure the force applied to the sensor by means of a square glass probe attached to a controllable linear stage. Forces from 0 to 12 N were systematically applied on the sensors to obtain loading and unloading characteristics, whereas a cyclic force of 3 N was applied to observe the stability of the sensors. The output of each sensor was logged using an E4980AL LCR meter (Keysight Technologies, Santa Clara, CA, USA) by measuring the change in their resistance. The measurements were recorded in a personal computer (PC) using a custom-developed application in LabVIEW 2018 Robotics v18.0f2 (National Instruments, TX, USA). Demonstration of the repeatability of the sensor's output was carried out using an mbed LPC1768 platform, which is based on a 32-bit Arm Cortex-M3 microcontroller (MCU) model LPC1768 (NXP Semiconductors, Eindhoven, The Netherlands). Four 12-bit analog-to-digital (ADC) channels of the MCU, with conversion rates up to 200 kHz, continuously acquiring the signals from the sensors. An average of 50 samples was computed within the MCU to eliminate noise. A custom-made LabVIEW program was used as a graphical programming interface for visualization of the data coming from the MCU. The raw data digitalized by the 12-bit ADC integrated in the MCU were transmitted to the PC using serial communication with a baud rate of 9600 bps.

3.2.2. Characterization of the Actuating Module

The displacement profile of the actuator was carried out using a custom optical lever technique shown in Figure S1, Supporting Information. It consists of a pointed laser source firmly attached

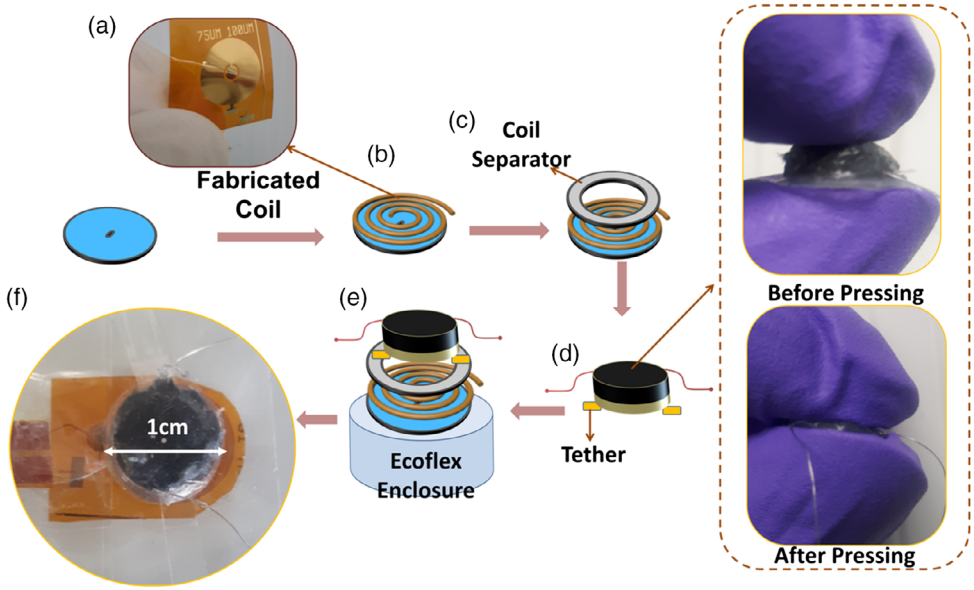

Figure 5. Integration of sensing and actuating elements; a) preparation of the polyimide sheet; b) attachment of the coil to the polyimide sheet; c) attachment of the coil separator to the coil; d) attachment of magnet tether to the embedded magnet; e) attachment of the piezoresistive layer and encapsulated magnet to the coil separator; and f) the integrated device (SensAct).

on an adjustable stand, a reflective mirror on the top of the actuator, a stable opaque screen, and a high-speed camera (960 frames per second [fps]) on a firm camera stand. The actuating module was driven with a signal generator, power supply, and a simple constant current drive circuit was used (Figure S1, Supporting Information). Preliminary preparation before the measurements involved directing the laser pointer onto the reflective mirror on top of the actuator with a proper adjustment to obtain sharp spot on the opaque screen and the camera was adjusted to properly capture the spot. During the characterization of the actuator in nonvibration state (both expansion and contraction modes), the actuator was driven with a constant current signal with 100% duty cycle, whereas during the vibration characterization the actuator was driven at the actuator's resonant frequency (40 Hz) and 50% duty cycle. When the current is turned on, the motion of the reflected laser on the screen is recorded with the camera. With proper calibration and using digital signal processing, the recorded video was processed by a MATLAB program to obtain the displacement of the actuator.

3.2.3. Characterization of the Integrated Sensing and Actuating Module

The performance of SensAct during simultaneous sensing and actuation was evaluated by applying a cyclic force of 2 N on the sensing layer using the same setup described in Section 3.2.1 and the schematic shown in Figure S3, Supporting Information. The resistance of the sensing layer was logged using an E4980AL LCR meter (Keysight Technologies, Santa Clara, CA, USA) while the current through the actuator was simultaneously measured using a digital multimeter and both measurements were recorded.

4. Results and Discussion

4.1. Performance of the piezoresistive Sensors

Figure 6a shows the loading and unloading characteristics of the four fabricated piezoresistive sensing elements using a contact force between 0 and 12 N.

Considering all four sensors in Figure 6a, the sensors have a mean variation of $\Delta R/R_o \approx 70\%$ around 5 N, with a standard deviation of ≈8.9%. This deviation in the response of all four sensors was found to be more significant after 2 N. From these values, the coefficient of variation (CV), which is used as a measure of the sensor's repeatability is ≈12.7% for all the sensors at 2 N. Considering sensor-to-sensor (sensor 1–4) variation, sensor 2 has the greatest standard deviation (≈13.64%), followed by sensor 4 (≈4.52%) and the least is sensor 3(≈1.46%) in comparison with sensor 1 (which has the highest resistance variation $\Delta R/R_o \approx 72\%$). During loading, the sensors experienced saturation when the applied force approached 5 N, and this is due to the graphite particles being almost completely in contact with one another when pressed; hence no significant change in resistance is experienced. During unloading, there is some hysteric effect (<10% average variation for applied forces <2.5 N) due to the viscoelastic creep inherent in the soft material (Sil-Poxy) used to encapsulate the sensing element (Figure 3). Consequently, the response of the sensor during unloading did not perfectly align with its loading characteristics. Figure 6b shows the cyclic loading of the four fabricated sensors with a force of 3 N. This resulted in an average resistance variation of $\Delta R/R_o \approx 45\%$ with a standard deviation of ≈3.2% and a reponse time of ≈149 ms. The demonstration of the sensor's performance and repeatability is shown in Video S1, Supporting Information.

4.2. Performance of the Actuating Module

This section presents the results of characterizing the actuating module of SensAct in different modes and states, as shown in **Figure 7**. The SensAct can operate in two actuation modes—contraction mode or expansion mode (Figure 7a); and also, in two states—nonvibration and vibration states (Figure 7b) depending on the magnitude and direction of current. Figure 7c,d shows the ability (including magnitude and direction) of the actuated layer (in nonvibration state) to stay in actuated positions during expansion and contraction modes respectively. From Figure 7c, when the actuator is turned on (point R) with ≈10 mA current, expansion takes place and the sensing (and magnetic) layer moves from point R to S

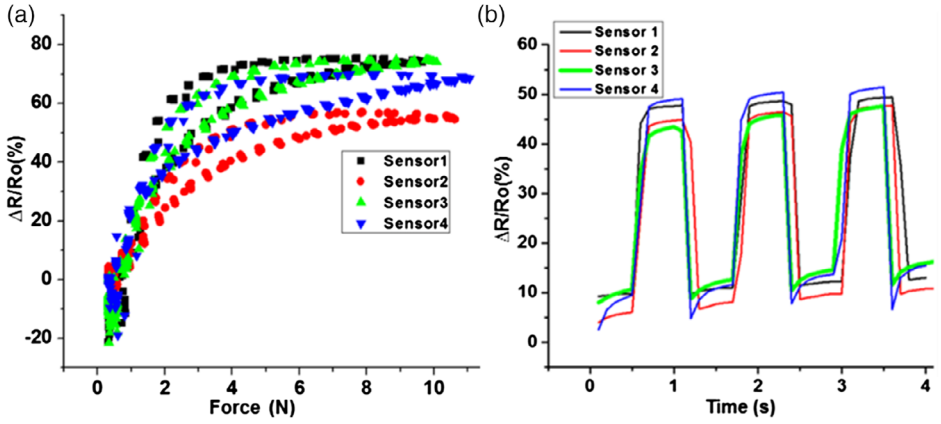

Figure 6. a) Loading and unloading characteristics for the four fabricated piezoresistive sensing layers; b) cyclic loading of the sensors using 3 N force at 0.8 Hz.

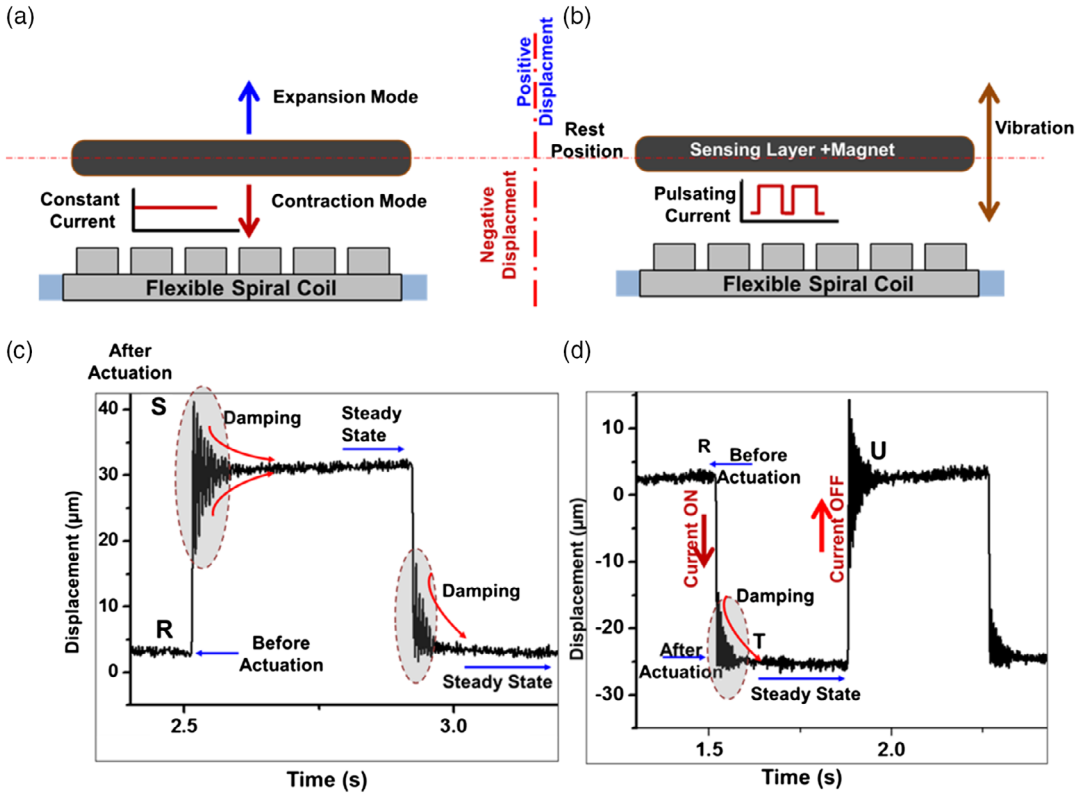

Figure 7. a) Description of the actuator modes: expansion and contraction; b) description of the vibration state; c) displacement profile for expansion mode at ≈10 mA constant current; d) displacement profile for both contraction mode at ≈10 mA constant current.

(≈38 μm). Damping occurs for ≈0.1 s before it settles to the new actuated position (at ≈+25 μm displacement with reference to point R) and is allowed to stay there for the next 0.3 s. Now, when the supply is turned off, the sensing (and magnetic) layer returns to the rest position (R) after experiencing ≈0.1 s damping and then settles to an almost steady state. Although the actuator experienced more damping in moving from point R to S in comparison with S to R, the settling time (≈0.1 s) is approximately the same in each case.

The response profile of the actuator for contraction mode using ≈10 mA drive current is shown in Figure 7d. When the direction of the actuating current is reversed (opposite to that used for expansion mode) and turned on (point R—Figure 7d), the sensing (and magnetic) layer experiences a negative is displacement ≈−25 μm (from point R to T) with reference to the rest position point R. Damping occurred immediately after it reached point T for −0.08 s before settling to its new position (T). When the current is turned off, the sensing (and magnetic) layer, moves from point T to point U after another damping. So, by changing the direction of current and holding it either in on or off state, the position of the sensing and magnetic layer is manipulated accordingly. The profile of the actuating layer in nonvibration state for some other current values up to 48 mA in expansion mode is shown in **Figure 8**a. It shows that the actuator can be conveniently actuated at different currents (1–48 mA) in the same way, as previously shown in Figure 7c,d.

The profile of the actuating layer in vibration state at 40 Hz is shown in Figure 8b. It should be noted that for vibration and nonvibration states, the displacement increases with increasing current. This is further shown in the current–displacement profile of the actuator shown in Figure 8c. As expected, the displacement increases proportionally with current, and ranges from ≈2.3 μm for 1 mA, up to ≈69.8 μm for 48 mA during nonvibration state. In the case of vibration state (Figure 8b), the displacement varied from ≈3 μm for 1 mA up to ≈111.8 μm for 48 mA.

4.3. Performance of SensAct during Simultaneous Sensing and Actuation

Figure 9 shows the performance of SensAct during simultaneous sensing and actuation including the corresponding change in current and actuation for different applied forces (0–2 N) on the sensing layer.

The sensing layer could be used to modulate the actuation; hence when a force is applied on the sensing layer, a proportional current flow through the actuator causing a corresponding change in the displacement of the sensing layer.

Figure 9a–c shows the stability of the change in current ($\Delta I/I_o$) through the actuator for different change in resistances ($\Delta R/R_o$) of the sensing layer for an applied cyclic force of 2 N. In each case, for a variation of $\Delta R/R_o$ ≈14% in the sensing layer, there is $\Delta I/I_o$ ≈500% change in the current through the actuator. This is a significant change and shows that the actuation of

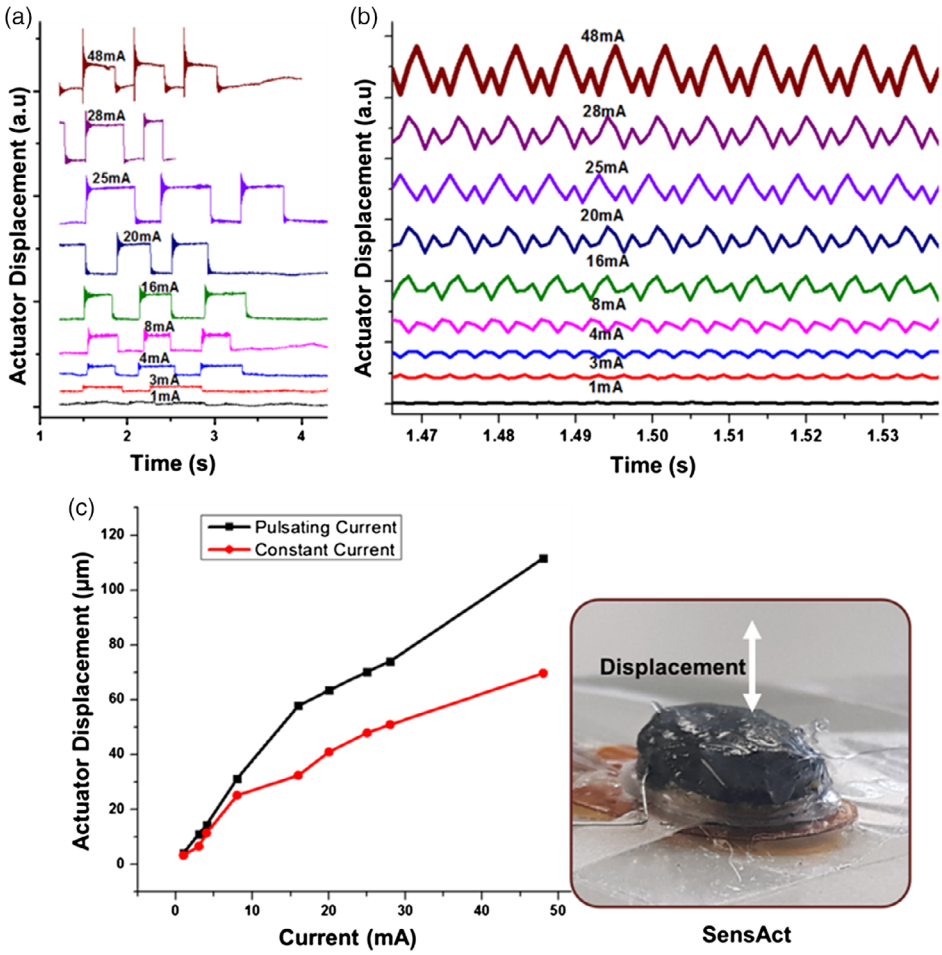

Figure 8. a) Displacement profile of SensAct for expansion mode using 1, 3, 4, 8, 16, 20, 25, 28, and 48 mA constant current; b) vibration profile of SensAct at 40 Hz and 1, 3, 4, 8, 16, 20, 25, 28, and 48 mA pulsating current; c) displacement profile of the actuator for different current values.

SensAct could be stably modulated by tuning the resistance layer at different frequencies. Figure S2c, Supporting Information, shows the stability of the actuating current during simultaneous sensing and actuation for ≈22 min. Figure 9d shows the response of SensAct when a force between 0 and 2 N is applied to the sensing layer. When this occurs, the resistance of the sensing layer changes ($\Delta R/R_o \approx 14\%$), and this change is used to modulate the current ($\Delta I/I_o \approx 385\%$ for 2 N on sensing layer) flowing through the coil thereby modulating the actuation of the sensing layer.

5. Application

In this section, the possibility of using the fabricated device for controllable vibrotactile feedback in prosthesis is demonstrated. The fabricated sensing layer was systematically embedded in a prosthetic finger and wirelessly used to control SensAct in a vibration state. **Figure 10** shows the scheme utilized for embedding one of the soft piezoresistive sensors into the fingertip of a custom 3D-printed prosthetic hand as a proof of concept. First a 3D computer-aided design (CAD) model (Figure 10a1,a2) of the required fingertip was designed to fit into the custom 3D-printed hand. The CAD model was designed to fit into the cavities of the distal phalanx of the thumb (Part A). In the interior of the design are channels connected to basic electronic components required for reading the resistance value of the sensor. The piezoresistive sensor (Figure 10a3) was encapsulated by the second part of the model (part B). The designed model for part A and part B was then printed separately with rigid and soft materials, respectively (Figure 10a1,a2). Part A was printed with Black PLA (RS components) using a nozzle of 0.4 mm diameter, 100% infill, and 0.1 mm layer height. The nozzle and the heated bed temperatures were 200 and 60 °C, respectively. In the core of part A (Figure 10a1), there is a cavity designed for embedding a resistor which is needed to read the value of the piezoresistive pressure sensor. To achieve this, the Gcode was modified to pause the print around the 100th layer. At this point, the resistor was placed in the cavity and the printing was resumed.

The Part B (Figure 10a2) for the sensor was printed with thermoplastic polyurethane (TPU) (NinjaFlex, NinjaTech) at a temperature of 235 °C with a 60% infill. TPU is a flexible elastomer highly suitable for replicating the stiffness and

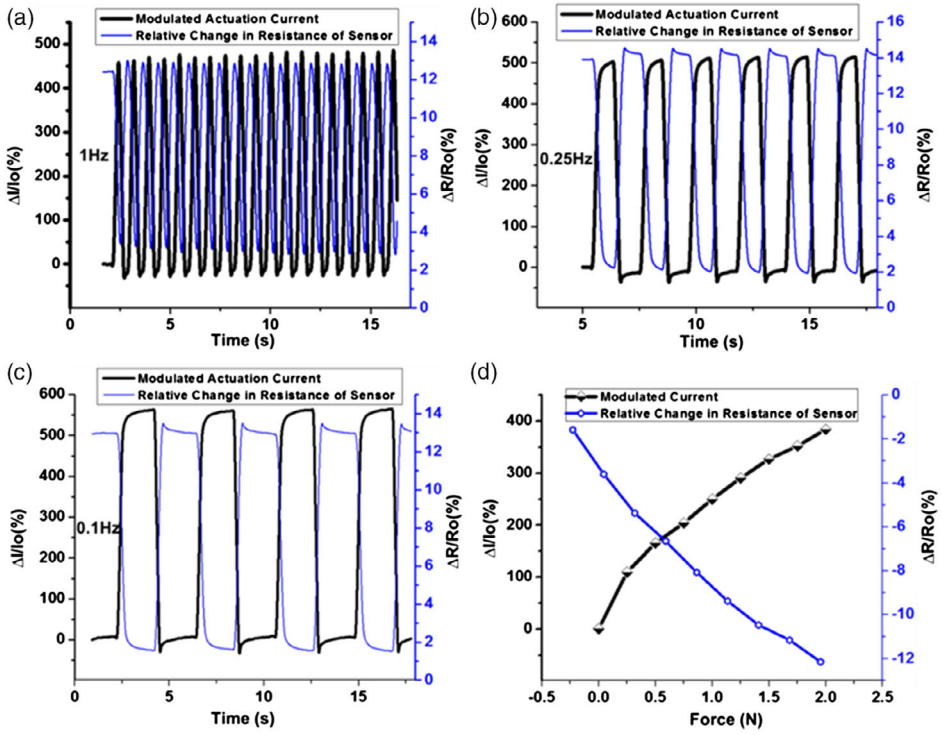

Figure 9. Modulated current driving the actuator during a cyclic loading of the sensing layer at different frequencies and the actuator driven at 100% duty cycle: a) 1 Hz; b) 0.25 Hz; and c) 0.1 Hz; d) Response profile of SensAct during simultaneous sensing and actuation from 0 to 2 N.

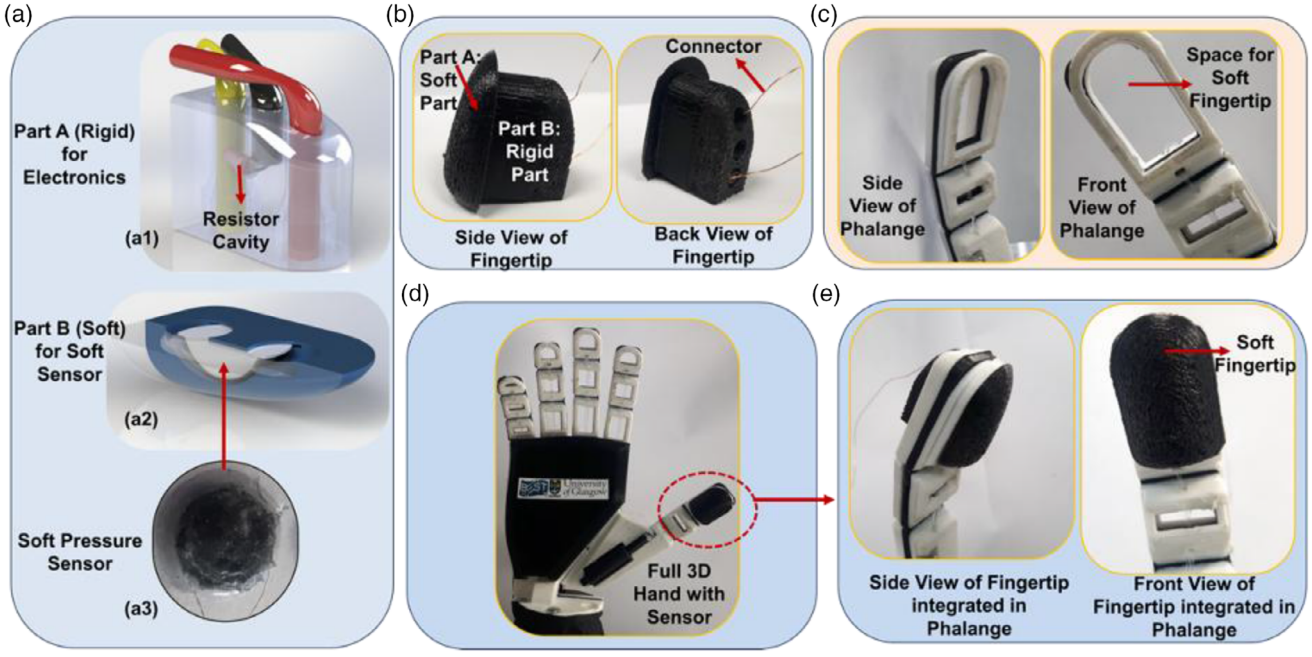

Figure 10. a) 3D Model of the fingertip and soft piezoresistive sensor; b) the fabricated 3D-printed fingertip with embedded sensor; c) Phalange of the custom 3D-printed hand with provision for integrating the sensorized fingertip; d) full custom 3D-printed hand with the sensorized fingertip attached; e) zoom in of the integrated fingertip.

elasticity of the skin. In this case, the GCode was also modified to pause at the 27th layer for the placement of the sensor. After embedding the sensor, the printing flow rate was tuned from 100% to 99% to reduce the infill line width to further improve the compressibility. Finally, the two parts were glued together with Epoxy and attached to the robotic hand (Figure 10e).

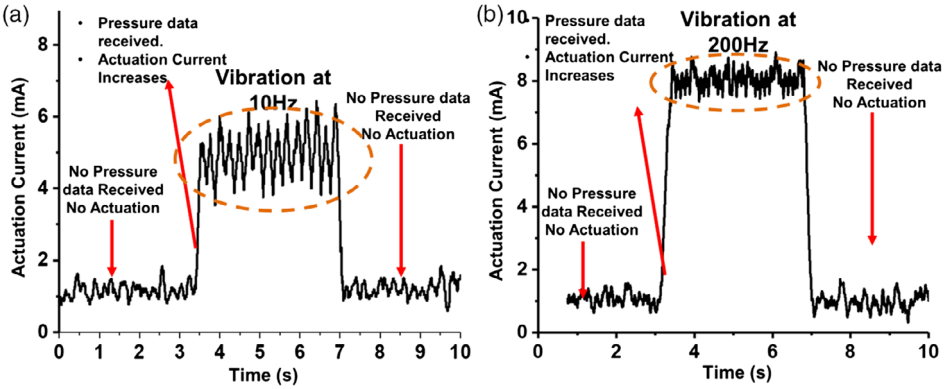

Figure 11. Response of the actuator upon reception of wireless pressure information; a) actuation at 10 Hz and b) actuation at 200 Hz.

The demonstration 3D-printed hand with embedded piezoresistive sensor is shown in Video S3, Supporting Information.

To demonstrate the capability of SensAct to provide vibrotactile feedback, the piezoresistive sensor was used to wirelessly control SensAct in its vibration state. Details of the circuit interface used for this is shown in Figure S4, Supporting Information. Through a MCU (32-bit Arm Cortex-M3 MCU model LPC1768 [NXP Semiconductors, Eindhoven, The Netherlands]), the measured resistance corresponding to the amount of applied force is wirelessly transmitted to the actuation module (of SensAct), which vibrates according to the level of pressure from the remote sensor. Bluetooth communication protocol was used to establish the connection between the sensing and the actuation modules, and the real-time response of the actuation element was recorded upon receipt of wireless pressure information. LabVIEW was used at the receiving end as a graphical programming interface to visualize the amount of current flowing through the actuator during vibration.

As shown in **Figure 11**, this current is proportional to the amount of real-time force produced at the remote location and is responsible for modulation of the vibration in the actuator. Figure 11a,b shows the response of SensAct during wireless transmission of pressure data via Bluetooth for pressure-mapped remote vibrotactile feedback at 10 and 200 Hz, respectively. When an external force is applied on the sensor, the pressure data are transmitted via Bluetooth to the actuating element in SensAct thereby creating proportional current through the actuator and hence vibration. When the external force of ≈2 N is applied on the sensor with the controllable linear stage with attached square probe, the current through the receiving coil pulsates from high to low, as shown by the dotted oval shape in Figure 11a,b in accordance with the vibration frequency (10 and 200 Hz, respectively). So apart from SensAct's potential for controllable eSkin application, the demonstrated vibrotactile feedback is advantageous for close loop control in prosthesis as well as for communication between deaf-blind people.[4b,25]

6. Conclusion

In this article, we presented SensAct, a device with soft tactile sensor and flexible actuator capable of self-controlled simultaneous sensing and actuation. The sensing layer is based on a piezoresistive sensor. At 5 N, four such sensors fabricated in this work gave $\Delta R/R_o \approx 70\%$ and standard deviation of 8.9%; this gives a coefficient of variation of ≈12.7% and hence good repeatability. The actuation module is a magnet driven by a flexible spiral coil and so operates in two different modes (contraction and expansion) and two different states (vibration and nonvibration states) depending on the magnitude and direction of the drive current. Both actuation and sensing layers can work simultaneously together and a force of 2 N applied on the sensing layer produced a variation of $\Delta I/I_o \approx 385\%$ in the actuation current. By systematically embedding the sensor in a custom 3D-printed hand, we demonstrated the use of SensAct in its vibration state for application in wireless vibrotactile feedback, which can be used for restoration of feeling to amputees or for remote communication between deaf-blind people or a human and robot. In general, the self-controllability characteristic of SensAct and its performance makes the concept advantageous for use in future tunable eSkin, enabling controllability and the extraction of richer information. The performance of SensAct during simultaneous sensing and actuation is demonstrated in Video S2, Supporting Information.

Supporting Information

Supporting Information is available from the Wiley Online Library or from the author.

Acknowledgements

This work was supported in part by Engineering and Physical Sciences Research Council (EPSRC) Fellowship for Growth (EP/M002527/1 and EP/R029644/1) and the European Commission through Future Emerging Technologies project PH-CODING (H2020-FETOPEN-2018-829186) and Marie Curie Fellowship FLEXI-G (H2020-MSCA-IF-2017-798639).

Conflict of Interest

The authors declare no conflict of interest.

Keywords

flexible actuators, haptics, SensAct, soft touch sensors, tactile sensing

Received: November 13, 2019
Revised: December 15, 2019
Published online:

[1] a) C. García Núñez, L. Manjakkal, R. Dahiya, *npj Flexible Electron.* **2019**, *3*, 1; b) R. Dahiya, *Proc. IEEE* **2019**, *107*, 247; c) S. Luo, J. Bimbo, R. Dahiya, H. Liu, *Mechatronics* **2017**, *48*, 54; d) R. Dahiya, W. Taube, S. Khan, E. Polat, *Inf. Display* **2015**, 31; e) R. Dahiya, N. Yogeswaran, F. Liu, L. Manjakkal, E. Burdet, V. Hayward, H. Jörntell, *Proc. IEEE* **2019**, *107*, 2016.

[2] G. M. Whitesides, *Angew. Chem., Int. Ed.* **2018**, *57*, 4258.

[3] a) A. Chortos, J. Liu, Z. Bao, *Nat. Mater.* **2016**, *15*, 937; b) A. Polishchuk, W. T. Navaraj, H. Heidari, R. Dahiya, *Procedia Eng.* **2016**, *168*, 1605; c) M. Ntagios, H. Nassar, A. Pullanchiyodan, W. T. Navaraj, R. Dahiya, *Adv. Intell. Syst.* **2020**, *2*, 1900080.

[4] a) H. Kou, L. Zhang, Q. Tan, G. Liu, H. Dong, W. Zhang, J. Xiong, *Sci. Rep.* **2019**, *9*, 3916; b) O. Ozioko, W. Navaraj, M. Hersh, R. Dahiya, *Sensors* **2020**, *20*, 4780.

[5] N. Yogeswaran, W. Dang, W. T. Navaraj, D. Shakthivel, S. Khan, E. O. Polat, S. Gupta, H. Heidari, M. Kaboli, L. Lorenzelli, *Adv. Robot.* **2015**, *29*, 1359.

[6] a) S. C. Mannsfeld, B. C. Tee, R. M. Stoltenberg, C. V. H. Chen, S. Barman, B. V. Muir, A. N. Sokolov, C. Reese, Z. Bao, *Nat. Mater.* **2010**, *9*, 859; b) S. Gong, W. Schwalb, Y. Wang, Y. Chen, Y. Tang, J. Si, B. Shirinzadeh, W. Cheng, *Nat. Commun.* **2014**, *5*, 3132; c) X. Wang, Y. Gu, Z. Xiong, Z. Cui, T. Zhang, *Adv. Mater.* **2014**, *26*, 1336.

[7] a) W. Taube Navaraj, C. García Núñez, D. Shakthivel, V. Vinciguerra, F. Labeau, D. H. Gregory, R. Dahiya, *Front. Neurosci.* **2017**, *11*, 501; b) R. S. Dahiya, M. Gori, *J. Neurophysiol.* **2010**, *104*, 1; c) W. Navaraj, R. Dahiya, *Adv. Intell. Syst.* **2019**, *1*, 1900051.

[8] a) T. Kawasetsu, T. Horii, H. Ishihara, M. Asada, *IEEE Sens. J.* **2018**, *18*, 5834; b) R. S. Dahiya, M. Valle, *Robotic Tactile Sensing: Technologies and System*, Springer, Dordrecht **2013**; c) S. Gupta, D. Shakthivel, L. Lorenzelli, R. Dahiya, *IEEE Sens. J.* **2018**, *19*, 435; d) N. Yogeswaran, W. Navaraj, S. Gupta, F. Liu, V. Vinciguerra, L. Lorenzelli, R. Dahiya, *Appl. Phys. Lett.* **2018**, *113*, 014102; e) S. Hannah, A. Davidson, I. Glesk, D. Uttamchandani, R. Dahiya, H. Gleskova, *Org. Electron.* **2018**, *56*, 170; f) S. Khan, W. Dang, L. Lorenzelli, R. Dahiya, *IEEE Trans. Semicond. Manuf.* **2015**, *28*, 486; g) A. Adami, R. S. Dahiya, C. Collini, D. Cattin, L. Lorenzelli, *Sens. Actuators, A* **2012**, *188*, 75; h) R. S. Dahiya, D. Cattin, A. Adami, C. Collini, L. Barboni, M. Valle, L. Lorenzelli, R. Oboe, G. Metta, F. Brunetti, *IEEE Sens. J.* **2011**, *11*, 3216; i) S. Gupta, N. Yogeswaran, F. Giacomozzi, L. Lorenzelli, R. Dahiya, *IEEE Sens. J.* **2019**, *20*, 6810.

[9] C. G. Núñez, W. T. Navaraj, E. O. Polat, R. Dahiya, *Adv. Funct. Mater.* **2017**, *27*, 1606287.

[10] M. Soni, R. Dahiya, *Philos. Trans. R. Soc. A* **2020**, *378*, 20190156.

[11] M. Roger, N. Fullard, L. Costello, S. Bradbury, E. Markiewicz, S. O'Reilly, N. Darling, P. Ritchie, A. Määttä, I. Karakesisoglou, *J. Anat.* **2019**, *234*, 438.

[12] a) B. Andò, V. Marletta, *Actuators* **2016**, *5*, 1; b) T. N. Do, H. Phan, T. Q. Nguyen, Y. Visell, *Adv. Funct. Mater.* **2018**, *28*, 1800244.

[13] J. C. Yeo, H. K. Yap, W. Xi, Z. Wang, C. H. Yeow, C. T. Lim, *Adv. Mater. Technol.* **2016**, *1*, 1600018.

[14] K. Kruusamäe, A. Punning, A. Aabloo, K. Asaka, *Actuators* **2015**, *4*, 17.

[15] L. Chen, M. Weng, P. Zhou, F. Huang, C. Liu, S. Fan, W. Zhang, *Adv. Funct. Mater.* **2019**, *29*, 1806057.

[16] a) K. Asaka, K. Mukai, T. Sugino, K. Kiyohara, *Polym. Int.* **2013**, *62*, 1263; b) K. Jung, K. J. Kim, H. R. Choi, *Sens. Actuators, A* **2008**, *143*, 343.

[17] S. Biswas, Y. Visell, *Adv. Mater. Technol.* **2019**, *4*, 1900042.

[18] O. Ozioko, P. Karipoth, M. Hersh, R. Dahiya, *IEEE Trans. Neural Syst. Rehabil. Eng.* **2020**, *28*, 1344.

[19] a) T. Hellebrekers, O. Kroemer, C. Majidi, *Adv. Intell. Syst.* **2019**, *1*, 1900025; b) A. S. Almansouri, N. A. Alsharif, M. A. Khan, L. Swanepoel, A. Kaidarova, K. N. Salama, J. Kosel, *Adv. Mater. Technol.* **2019**, *4*, 1900493; c) C. Hintze, D. Borin, D. Ivaneyko, V. Toshchevikov, M. Saphiannikova-Grenzer, G. Heinrich, *KGK Kautsch. Gummi Kunstst.* **2014**, *67*, 53.

[20] a) A. A. Paknahad, M. Tahmasebipour, *Microelectron. Eng.* **2019**, 111031; b) M. M. Said, J. Yunas, R. E. Pawinanto, B. Y. Majlis, B. Bais, *Sens. Actuators, A* **2016**, *245*, 85.

[21] M. Mohd Said, J. Yunas, B. Bais, A. A. Hamzah, B. Yeop Majlis, *Micromachines* **2018**, *9*, 13.

[22] J. J. Zárate, H. Shea, *IEEE Trans. Haptic.* **2016**, *10*, 106.

[23] O. Ozioko, M. Hersh, R. Dahiya, *presented at 2018 IEEE Sensors*, New Delhi, India, October **2018**.

[24] M. Schlesinger, M. Paunovic, *Modern Electroplating*, Wiley, New York/ Chichester, UK **2011**.

[25] A. Erwin, F. C. Sup IV, *PLoS One* **2015**, *10*, e0134095.